The origins and impact of outflow from super-Eddington flow

Takaaki KITAKI**,**[1,*] **Shin M**INESHIGE**,**[1] **Ken O**HSUGA**,**[2]
and Tomohisa KAWASHIMA[3]

[1]Department of Astronomy, Graduate School of Science, Kyoto University, Kitashirakawa-Oiwake-cho,
 Sakyo-ku, Kyoto, Kyoto 606-8502, Japan
[2]Center for Computational Sciences, University of Tsukuba, 1-1-1 Ten-nodai, Tsukuba, Ibaraki 305-8577,
 Japan
[3]Institute for Cosmic Ray Research, The University of Tokyo, 5-1-5 Kashiwanoha, Kashiwa, Chiba 277-8582,
 Japan

*E-mail: kitaki@kusastro.kyoto-u.ac.jp

Abstract

It is widely believed that super-Eddington accretion flow can produce powerful out-flow, but where does this originate and how much mass and energy are carried away in which directions? To answer these questions, we perform a new large-box, two-dimensional radiation hydrodynamic simulation, paying special attention lest the results should depend on the adopted initial and boundary conditions. We achieve a quasi-steady state at an unprecedentedly large range, $r = 2$–$600 r_S$ (with r_S being the Schwarzschild radius), from the black hole. The accretion rate onto the central $10 M_\odot$ black hole is $\dot{M}_{BH} \sim 180 L_{Edd}/c^2$, whereas the mass outflow rate is $\dot{M}_{outflow} \sim 24 L_{Edd}/c^2$ (where L_{Edd} and c are the Eddington luminosity and the speed of light, respectively). The ratio $\dot{M}_{outflow}/\dot{M}_{BH} \sim 0.14$ is much less than previously reported. By careful inspection we find that most of the outflowing gas reaching the outer boundary originates from the region at $R \lesssim 140 r_S$, while gas at 140–$230 r_S$ forms failed outflow. Therefore, significant outflow occurs inside the trapping radius $\sim 450 r_S$. The mechanical energy flux (or mass flux) reaches its maximum in the direction of $\sim 15°$ ($\sim 80°$) from the rotation axis. The total mechanical luminosity is $L_{mec} \sim 0.16 L_{Edd}$, while the isotropic X-ray luminosity varies from $L_X^{ISO} \sim 2.9 L_{Edd}$ (for a face-on observer) to $\sim 2.1 L_{Edd}$ (for a nearly edge-on observer). The power ratio is $L_{mec}/L_X^{ISO} \sim 0.05$–$0.08$, in good agreement with observations of ultra-luminous X-ray sources surrounded by optical nebulae.

Key words: accretion, accretion disks — radiation: dynamics — stars: black holes

1 Introduction

It is well known that gas accretion onto a black hole produces enormous energy, giving rise to a variety of active phenomena in black hole objects, such as X-ray binaries and active galactic nuclei. The gas in the accretion disk falls onto the central black hole via transportation of the angular momentum by the viscosity, and releases gravitational energy in the forms of radiation energy and/or mechanical energy (see, e.g., Shakura & Sunyaev 1973). There is a classical limit to the total amount of radiation

energy released per unit time by accretion; that is what we call the Eddington luminosity, L_{Edd}. It is derived from the balance between the radiation force and the gravitational force under spherical symmetry, and is written as

$$L_{Edd} \equiv \frac{4\pi c G M_{BH}}{\kappa_{es}} \simeq 1.26 \times 10^{39} \left(\frac{M_{BH}}{10 \, M_\odot}\right) \, \text{erg s}^{-1}. \quad (1)$$

Here, c is the speed of light, G is the gravitational constant, M_{BH} is the mass of the central black hole, κ_{es} is the Thomson scattering opacity, and we have assumed the hydrogen abundance of $X = 1.0$.

It is now widely accepted that the classical limit can be exceeded in disk accretion because of the separation of the directions of the gas inflow and the radiation output. Super-Eddington accretion flow is gas flow with extremely high accretion rates, $\dot{M}_{BH} \gg L_{Edd}/c^2$, and is known to shine at the super-Eddington luminosity. Several astrophysical objects are known to harbor super-Eddington accretors; good candidates are ultra-luminous X-ray sources (ULXs), and some microquasars (e.g., GRS 1915+105) and narrow-line Seyfert 1 galaxies (NLS1s; e.g., Mineshige et al. 2000; Jin et al. 2017).

ULXs are bright X-ray compact sources whose X-ray luminosity is 10^{39}–10^{41} erg s^{-1} and have been discovered in off-nuclear regions of nearby galaxies (see Kaaret et al. 2017 for a recent review). There are two main ideas to explain high luminosity: one is sub-Eddington accretion onto intermediate-mass black holes (IMBH; Makishima et al. 2000; Miller et al. 2004), and the other is super-Eddington accretion onto stellar-mass black holes (Watarai et al. 2001; King et al. 2001).

The situation changed drastically after the discovery of the so-called ULX pulsars as a subgroup of ULXs showing periodic X-ray pulses (e.g., M 82 X-2, Bachetti et al. 2014; NGC 7793 P13, Fürst et al. 2016; Israel et al. 2017). Now they are known to possess magnetized neutron stars. These discoveries support the super-Eddington accretion scenario, although there still remains room for the IMBH hypothesis to survive to account for the extremely high luminosity of hyper-luminous X-ray sources (see, e.g., Barrows et al. 2019 and references therein).

From the theoretical point of view, one of the most prominent features of super-Eddington accretion flow is the photon-trapping effect (Katz 1977; Begelman 1978; Abramowicz et al. 1988). When the mass accretion rate is very large, $\dot{M} \gg L_{Edd}/c^2$, so is the vertical optical depth, τ_e ($= \kappa_{es}\Sigma$, with Σ being the surface density), since we have $\dot{M} = 2\pi r \Sigma |v_r|$ (with v_r being the radial velocity). Then, the photon diffusion timescale ($\propto \tau_e$) to the disk surface can exceed the accretion timescale ($= r/|v_r|$). When this occurs, photons will be trapped within gas flow and

swallowed by a central black hole together with the gas. The photon-trapping radius R_{trap} inside which the photon-trapping effect is significant is given (see, e.g., Kato et al. 2008) by

$$R_{trap} = \frac{3}{2} \frac{H}{R} \dot{m}_{BH} r_S. \quad (2)$$

Here, H is the scale-height of the accretion disk, R is the radius in cylindrical coordinates, $\dot{m}_{BH} \equiv \dot{M}_{BH}/(L_{Edd}/c^2)$ is the normalized mass accretion rate onto the black hole, and $r_s \equiv 2GM_{BH}/c^2$ is the Schwarzschild radius.

Outflow is another prominent feature of super-Eddington accretion flow. The super-Eddington luminosity implies that the radiation force is greater than the gravitational force, leading to the emergence of radiation-pressure-driven outflow (Shakura & Sunyaev 1973). Once gas is blown away from the disk surface in the form of outflow, it will inevitably have an impact on environments far from the central black hole. The accretion disk structure itself should also be affected, since the accretion rate within the disk is no longer constant in space. Moreover, the emergent spectrum will be modified via Comptonization by the outflowing gas (Kawashima et al. 2012; Kitaki et al. 2017; Narayan et al. 2017). This will account for the observed spectra in the so-called ultra-luminous state of ULXs (Gladstone et al. 2009; Kawashima et al. 2012).

We can derive the launching radius by considering the balance between the radiation force and the gravitational force at the disk surface; that is,

$$R_{lau} \sim A_{lau} \dot{m}_{BH} r_S. \quad (3)$$

Here, A_{lau} is a constant of order unity, depending on the geometry. The launching radius is essentially the same as those introduced in past studies but with different terminologies. In the spherization radius introduced by Shakura and Sunyaev (1973), for example, A_{lau} was taken to be unity, while $A_{lau} \sim 1.95$ in the critical radius introduced by Fukue (2004). We wish to note that the launching radius is crudely equal to the photon-trapping radius.

Although (semi-)analytical approaches are useful in understanding the basics of super-Eddington flow, we also need simulation studies to see what actually happens as a consequence of complex radiation–matter interactions. Multidimensional RHD (radiation hydrodynamic) simulations of super-Eddington accretion flow were pioneered by Eggum, Coroniti, and Katz (1988), followed by Fujita and Okuda (1998). Their 2D (two-dimensional) RHD simulations have shown that super-Eddington accretion flow has a puffed-up structure and that high-speed outflow forms a funnel near the rotational axis. Those simulation studies

Table 1. Results and initial settings of simulations.[*]

Sources[†]	Method	Compton [Yes/No]	r_{out} [r_S]	r_K [r_S]	r_{qss} [r_S]	R_{trap} [r_S]	$\dot{M}_{BH}$ [L_{Edd}/c^2]	$\dot{M}_{outflow}$ [L_{Edd}/c^2]
Our simulation	2D-RHD	Yes	3000	2430	~600	~270	~180	~24
Ohsuga+05	2D-RHD	No	500	100	~30	~200	~130	
Ohsuga+11	2D-RMHD	No	105	40	~10	~150	~100	
Jiang+14	3D-RMHD	No	50	25	~20	~330	~220	~400
Sądowski+15	2D-GR-RMHD	Yes	2500	21	~35	~640	~420	~7000
Sądowski+16	3D-GR-RMHD	Yes	500	20	~10	~260	~180	~520
Hashizume+15	2D-RHD	No	5000	100	~100	~230	~150	~500
Takahashi+16	3D-GR-RMHD	No	125	17	~10	~300	~200	
Kitaki+18	2D-RHD	Yes	3000	300	~200	~420	~280	~300
Jiang+19	3D-RMHD	Yes	800	40	~15	~380	~250	

[*]Here, r_{out} is the radius at the outer boundary, r_K is the initial Keplerian radius, r_{qss} is the radius inside which the quasi-steady state is established, R_{trap} is the photon-trapping radius derived based on equation (2), $\dot{M}_{BH}$ is the accretion rate onto the black hole, and $\dot{M}_{outflow}$ is the outflow rate at around r_{out}. We also indicate whether or not the Compton scattering effect is taken into account.

[†]Sources: Hashizume+15: Hashizume et al. (2015); Jiang+14: Jiang, Stone, and Davis (2014); Jiang+19: Jiang Stone, and Davis (2019); Kitaki+18: Kitaki et al. (2018); Ohsuga+05: Ohsuga et al. (2005); Ohsuga+11: Ohsuga and Mineshige (2011); Sądowski+15: Sądowski et al. (2015); Sądowski+16: Sądowski and Narayan (2016); Takahashi+16: Takahashi et al. (2016).

were, however, restricted within small computational boxes due to the limits of the supercomputers available at the time.

More realistic and much larger-scale simulation studies were initiated by Ohsuga et al. (2005), who performed much longer-timescale simulations and clarified the detailed properties of the accretion flow, outflow, and the observational appearance of super-Eddington systems. Since then, extensive numerical simulation studies have been conducted, first in Newtonian dynamics (e.g., Ohsuga et al. 2009; Kawashima et al. 2009; Ohsuga & Mineshige 2011; Jiang et al. 2014, 2019) and then in general relativistic treatments (e.g., McKinney et al. 2014; Sądowski et al. 2015; Sądowski & Narayan 2016; Takahashi et al. 2016). In a rotating black hole, furthermore, the emergence of strong and powerful jets driven by the Blandford–Znajek mechanism (Blandford & Znajek 1977) is expected, which was calculated by GR-RMHD (general relativistic radiation magnetohydrodynamic) and GR-MHD (general relativistic magnetohydrodynamic) simulations.

We should note, however, that these authors adopted somewhat artificial numerical settings in these simulations for numerical reasons. To be more precise, they started simulations by putting an initial torus near a black hole or by injecting gas with small angular momentum so that a torus-like structure formed near a black hole.

There are certainly cases in which small r_K is expected, such as the case of tidal disruption events, but we focus on other cases with large r_K, bearing ULXs and NLS1s in mind. Here, we define the Keplerian radius, r_K, in such a way that the initial torus (with a given specific angular momentum) rotates around the central black hole with the Keplerian rotation velocity. We also define the quasi-steady radius r_{qss}, inside which a quasi-steady state is achieved (a more rigorous definition is given in subsection 3.2), and we list these values in table 1 for recent simulation studies. From this table we understand that both the Keplerian radius and the quasi-steady radius are smaller than the trapping radius R_{trap} [equation (2)] in all the previous simulations.

Both were required for numerical reasons, since otherwise it would take too much computational time to complete within a reasonable time, say, a few months. But we should point out that the previous simulation studies commonly exhibit a puffed-up structure near the black hole, since $r_K \ll R_{trap} \sim R_{lau}$, and that a large amount of outflow material originates from such an inflated zone. It may be possible that the outflow rate was grossly overestimated in such simulations (see table 1).

In the present study, therefore, we aim at expanding the quasi-steady region as much as possible so that it should cover the trapping radius and launching radius. With this issue kept in mind, we perform a 2D-RHD simulation of the super-Eddington accretion flow in a large calculation box, adopting a very large initial Keplerian radius (see table 1). The main objectives of the study are to clarify from which part of the accretion flow genuine outflow (that reaches the outer calculation boundary) is launched, and how much mass, momentum, and mechanical energy is carried away by outflow and in which direction. The plan of the paper is as follows: We first explain our numerical methods and models in the next section. We then present our results in section 3 and discuss them in section 4. The final section is devoted to conclusions.

2 Models and numerical methods

2.1 Radiation hydrodynamic simulations

We consider super-Eddington accretion flow and outflow onto a black hole by injecting mass from the outer simulation boundary at a constant rate of $\dot{M}_{\mathrm{input}}$ with angular momentum. The parameter values are specified in subsection 2.2. The flux-limited diffusion approximation is adopted (Levermore & Pomraning 1981; Turner & Stone 2001). We also adopt the α viscosity prescription (Shakura & Sunyaev 1973). General relativistic effects are incorporated by adopting the pseudo-Newtonian potential (Paczyński & Wiita 1980).

The basic equations and numerical methods are the same as those in Kitaki et al. (2017, 2018), but upgraded to solve the energy equations (see subsection 2.3). This 2D-RHD code solves the axisymmetric two-dimensional radiation hydrodynamic equations in the spherical coordinates $(x,\, y,\, z) = (r\sin\theta\cos\phi,\, r\sin\theta\sin\phi,\, r\cos\theta)$, where the azimuthal angle ϕ is set to be constant. We put a black hole of mass $10\, M_\odot$ at the origin. In this paper we distinguish r, the radius in spherical coordinates, and $R = \sqrt{x^2 + y^2}$, the radius in cylindrical coordinates [e.g., equation (2)].

The continuity equation is given by

$$\frac{\partial \rho}{\partial t} + \nabla \cdot (\rho \boldsymbol{v}) = 0, \tag{4}$$

where ρ is the gas mass density and $\boldsymbol{v} = (v_r, v_\theta, v_\phi)$ is the velocity of the gas. Note that we retain the azimuthal component of the velocity.

The equations of motion are written as

$$\frac{\partial (\rho v_r)}{\partial t} + \nabla \cdot (\rho v_r \boldsymbol{v}) = -\frac{\partial p}{\partial r} + \rho \left[\frac{v_\theta^2}{r} + \frac{v_\phi^2}{r} - \frac{GM_{\mathrm{BH}}}{(r - r_s)^2} \right]$$
$$+ \frac{\chi}{c} F_{0,r}, \tag{5}$$

$$\frac{\partial (\rho r v_\theta)}{\partial t} + \nabla \cdot (\rho r v_\theta \boldsymbol{v}) = -\frac{\partial p}{\partial \theta} + \rho v_\phi^2 \cot\theta + r\frac{\chi}{c} F_{0,\theta}, \tag{6}$$

$$\frac{\partial (\rho r \sin\theta v_\phi)}{\partial t} + \nabla \cdot (\rho r \sin\theta v_\phi \boldsymbol{v}) = \frac{1}{r^2} \frac{\partial}{\partial r} \left(r^3 \sin\theta t_{r\phi} \right). \tag{7}$$

Here, p is the gas pressure, $\chi = \kappa + \rho\sigma_{\mathrm{T}}/m_{\mathrm{p}}$ is the total opacity, where κ is the free–free and free–bound absorption opacity (Rybicki & Lightman 1979), σ_{T} is the Thomson scattering cross-section, m_{p} is the proton mass, and $\boldsymbol{F}_0 = (F_{0,r}, F_{0,\theta}, F_{0,\phi})$ is the radiative flux in the comoving frame, where the suffix 0 represents quantities in the comoving frame and we set $F_{0,\phi} = 0$.

We assume that only the r–ϕ component of the viscous-shear tensor is nonzero, and it is prescribed as

$$t_{r\phi} = \eta r \frac{\partial}{\partial r} \left(\frac{v_\phi}{r} \right), \tag{8}$$

with the dynamical viscous coefficient being

$$\eta = \alpha \frac{p + \lambda E_0}{\Omega_{\mathrm{K}}}. \tag{9}$$

Here, $\alpha = 0.1$ is the α parameter (Shakura & Sunyaev 1973), Ω_{K} is the Keplerian angular speed, E_0 is the radiation energy density, and λ represents the flux limiter of the flux-limited diffusion approximation (Levermore & Pomraning 1981; Turner & Stone 2001).

The gas and radiation energy equations are given by

$$\frac{\partial e}{\partial t} + \nabla \cdot (e\boldsymbol{v}) = -p\nabla \cdot \boldsymbol{v} - 4\pi\kappa B + c\kappa E_0$$
$$+ \Phi_{\mathrm{vis}} - \Gamma_{\mathrm{Comp}}, \tag{10}$$

and

$$\frac{\partial E_0}{\partial t} + \nabla \cdot (E_0 \boldsymbol{v}) = -\nabla \cdot \boldsymbol{F}_0 - \nabla \boldsymbol{v} : \mathbf{P}_0 + 4\pi\kappa B - c\kappa E_0$$
$$+ \Gamma_{\mathrm{Comp}}, \tag{11}$$

respectively. Here, e is the internal energy density, which is linked to the thermal pressure by the ideal gas equation of state, $p = (\gamma - 1)e = \rho k_{\mathrm{B}} T_{\mathrm{gas}}/(\mu m_{\mathrm{p}})$, with $\gamma = 5/3$ being the specific heat ratio, k_{B} the Boltzmann constant, $\mu = 0.5$ the mean molecular weight (we assume pure hydrogen plasmas), and T_{gas} the gas temperature. $B = \sigma_{\mathrm{SB}} T_{\mathrm{gas}}^4/\pi$ is the blackbody intensity, where σ_{SB} is the Stefan–Boltzmann constant. $\mathbf{P}_0$ is the radiation pressure tensor, and Φ_{vis} is the viscous dissipative function, written as

$$\Phi_{\mathrm{vis}} = \eta \left[r \frac{\partial}{\partial r} \left(\frac{v_\phi}{r} \right) \right]^2. \tag{12}$$

The Compton cooling/heating rate, Γ_{Comp}, is described as

$$\Gamma_{\mathrm{Comp}} = 4\sigma_{\mathrm{T}} c \frac{k_{\mathrm{B}} (T_{\mathrm{gas}} - T_{\mathrm{rad}})}{m_{\mathrm{e}} c^2} \left(\frac{\rho}{m_{\mathrm{p}}} \right) E_0. \tag{13}$$

Here, m_{e} is the electron mass and $T_{\mathrm{rad}} \equiv (E_0/a)^{1/4}$ is the radiation temperature with the radiation constant $a = 4\sigma_{\mathrm{SB}}/c$.

2.2 Initial conditions and calculated models

The simulation settings are also the same as in Kitaki et al. (2018) except for a larger value of r_{K} $(= 2430\, r_{\mathrm{S}})$. The computational box is set by $r_{\mathrm{in}} = 2\, r_{\mathrm{S}} \leq r \leq r_{\mathrm{out}} = 3000\, r_{\mathrm{S}}$, and $0 \leq \theta \leq \pi/2$. Grid points are uniformly distributed in logarithm in the radial direction, $\triangle\log_{10} r = (\log_{10} r_{\mathrm{out}} - \log_{10} r_{\mathrm{in}})/N_r$, and uniformly distributed in $\cos\theta$ in the polar

direction, $\triangle \cos\theta = 1/N_\theta$, where the numbers of grid points are $(N_r, N_\theta) = (200, 240)$. We also simulated the case with $(N_r, N_\theta) = (400, 480)$, confirming that our conclusions are not altered.

We initially put a hot, optically thin atmosphere with negligible mass around the black hole for numerical reasons. The initial atmosphere is assumed to be in isothermal hydrostatic equilibrium in the radial (r) direction. Then, the density profile is

$$\rho_{\rm atm}(r,\theta) \equiv \rho_{\rm out} \exp\left[\frac{\mu m_{\rm p} G M_{\rm BH}}{k_{\rm B} T_{\rm atm} r_{\rm out}} \left(\frac{r_{\rm out}}{r} - 1 \right) \right], \tag{14}$$

where $\rho_{\rm out}$ is the density at the outer boundary. We employ $\rho_{\rm out} = 10^{-17}\,{\rm g\,cm^{-3}}$ and $T_{\rm atm} = 10^{11}\,{\rm K}$, following Ohsuga et al. (2005).

Mass is injected continuously at a constant rate of $\dot{M}_{\rm input}$ through the outer disk boundary at $r = r_{\rm out}$, and $0.48\pi \leq \theta \leq 0.5\pi$. The black hole mass and mass injection rate are set to be $M_{\rm BH} = 10\,M_\odot$ and $\dot{M}_{\rm input} = 700\,L_{\rm Edd}/c^2$, respectively. The injected gas is assumed to possess a specific angular momentum corresponding to the Keplerian radius of $r_{\rm K} = 2430\,r_{\rm S}$ (i.e., the initial specific angular momentum is $\sqrt{G M_{\rm BH} r_{\rm K}}$). We thus expect that inflow material first falls towards the center and forms a rotating gaseous ring at around $r \sim r_{\rm K}$, from which the material slowly accretes inward via the viscous diffusion process. We allow mass to go out freely through the outer boundary at $r = r_{\rm out}$ and $0 \leq \theta \leq 0.48\pi$, and assume that mass at $r = r_{\rm in}$ is absorbed.

We assume that the density, gas pressure, radial velocity, and radiation energy density are symmetric at the rotational axis, while v_θ and v_ϕ are antisymmetric. On the equatorial plane, on the other hand, ρ, p, $v_{\rm r}$, v_ϕ, and E_0 are symmetric, and v_θ is antisymmetric. More details of the boundary conditions are given in Ohsuga et al. (2005).

2.3 Updating the energy equation solver

In this study we calculate the large-scale structure of the super-Eddington accretion flow by adopting the total energy equation instead of the internal energy equation. This is preferable for calculating large-scale flow structure, since total energy conservation does not hold in some cases if we use the internal energy equation.

We employ the operator-splitting method, in which the viscous processes are separated from other processes (i.e., advection, radiation). The viscosity-related terms in the equation of motion and energy equation are

$$\frac{\partial(\rho r \sin\theta v_\phi)}{\partial t} = \frac{1}{r^2} \frac{\partial}{\partial r} \left(r^3 \sin\theta\, t_{\rm r\phi} \right) \tag{15}$$
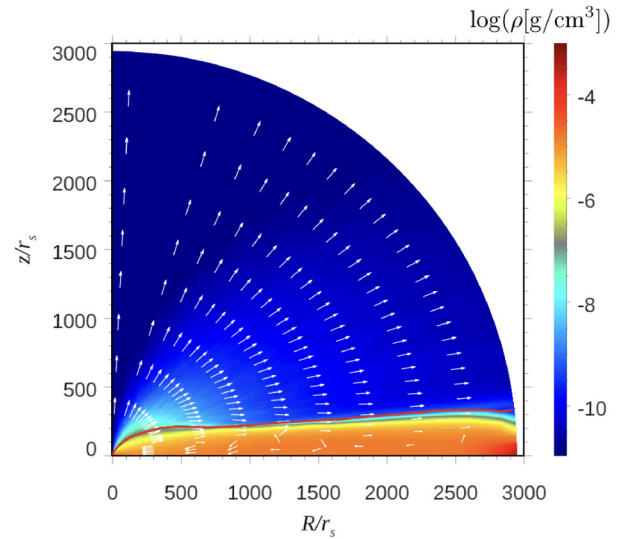

Fig. 1. Time-averaged density contours of super-Eddington accretion flow onto a black hole. Overlaid are the gas velocity vectors whose lengths are proportional to the logarithm of the absolute velocity. The red line represents the disk surface, which is defined as the loci where the radiation force balances the gravitational force. (Color online)

and

$$\frac{\partial}{\partial t} \left(e + \frac{1}{2} \rho v_\phi^2 \right) = \frac{1}{r^2} \frac{\partial}{\partial r} \left(r^2 t_{\rm r\phi} v_\phi \right), \tag{16}$$

respectively. We solve these equations in the following way: First, the equation of motion (15) is solved by the implicit method through the Thomas algorithm (e.g., Press et al. 2007), and the velocity in the next time step v_ϕ^{n+1} is calculated. Second, the total energy equation (16) is solved using the velocity v_ϕ^{n+1}, and the internal energy density in the next time step e^{n+1} is obtained. Then, other quantities will be updated. The advantage of this method is that the total energy is always conserved.

3 Results

3.1 Overall flow structure

In this paper we examine the time-averaged structure of both inflow and outflow in a quasi-steady state, unless stated otherwise. We first show, in figures 1 and 2, the density and temperature contours overlaid with the velocity fields in the quasi-steady state. All the physical quantities (i.e., temperature, velocity, etc.) except for gas mass density are time-averaged, weighted by the gas mass density during the interval $t \sim 8519$–9109 s, while the gas mass density is simple time averages with no weighting. After the simulation starts, the gas injected from the outer boundary into an initially empty zone first free-falls and accumulates around the initial Keplerian radius, $r_{\rm K} \sim 2430\,r_{\rm S}$, since the centrifugal force and the gravitational force balance
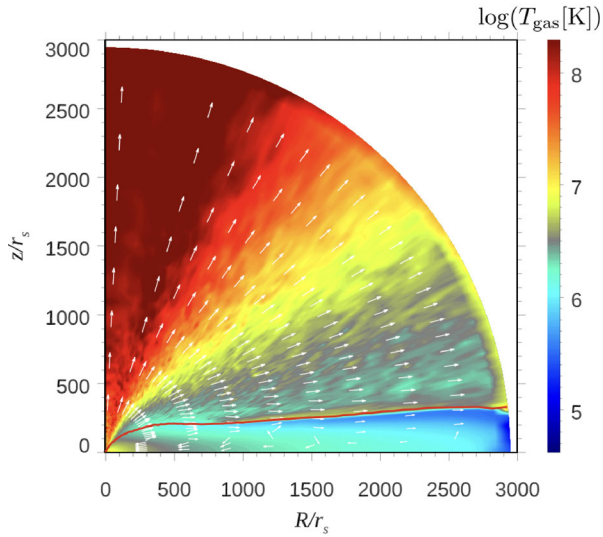
Fig. 2. As figure 1 but for the temperature contours. (Color online)

Fig. 3. Magnified view of the central region of figure 1. (Color online)

there. Soon after the transient initial phase, the accumulated matter spreads outward and inward in the radial direction via the viscous diffusion process, forming an accretion disk extending down to the innermost zone ($t \lesssim 8511\,\mathrm{s}$). The newly injected matter collides with the disk matter so that a high-density region appears at $\sim(2400\text{–}3000)\,r_\mathrm{S}$ (well outside the initial Keplerian radius); see figure 1. After a sufficiently long time (on the order of the viscous timescale, $t \gtrsim 8511\,\mathrm{s}$; Ohsuga et al. 2005), a quasi-steady inflow–outflow structure is established (see figure 1).

In figures 1 and 2 we also indicate the disk surface by a red solid line. By the disk surface we mean the loci on which radiation force balances the gravity in the radial direction, $\chi F_{0,r}/c = \rho G M_\mathrm{BH}/(r - r_\mathrm{S})^2$. We examined other definitions of the disk surface, for example by including the centrifugal force term, $\rho v_\phi^2/r$, but found no better definitions in a simple form.

We notice a quite different flow shape in figure 1 from those reported previously (see table 1). That is, we no longer find a puffed-up structure, which was commonly observed in the previous studies, but rather a smooth disk shape up to the outer boundary (see model a11 of figure 1 in Kitaki et al. 2018). This is because we adopted a much larger Keplerian radius than the previous simulations. The disk height is roughly proportional to R in the inner region, $R \lesssim 300\,r_\mathrm{S}$, whereas it is roughly constant outside ($H \sim 200\text{–}300\,r_\mathrm{S}$).

We also plot the velocity fields of gas by the white vectors in figures 1 and 2. We understand that gas is stripped off the disk surface to form outflow. Near the rotation axis, in particular, we see a cone-shaped funnel filled with high-velocity ($\sim 0.3\,c$) and high-temperature plasmas of $T_\mathrm{gas} \gtrsim 10^8\,\mathrm{K}$, surrounded by the outflow region of modest
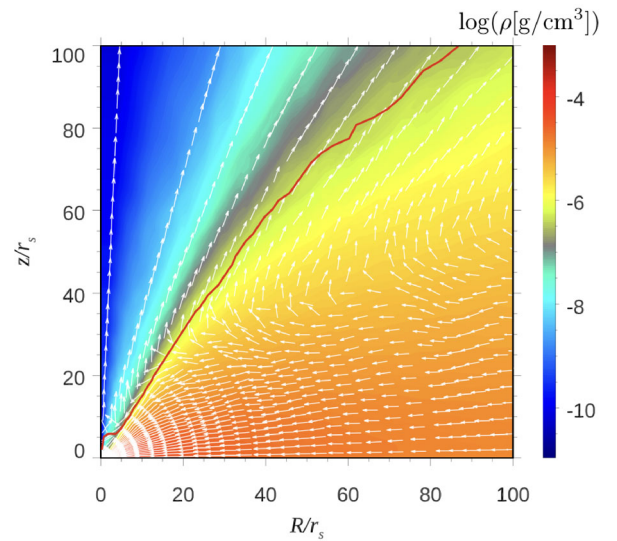
velocity ($\sim 0.05\text{–}0.1\,c$) and modest temperatures, $T_\mathrm{gas} \sim 10^{6-7}\,\mathrm{K}$.

Figure 3 is a magnification of the central region of figure 1. When we have a closer look at the disk region, we notice that the gas motion is outward near the surface, whereas it is inward near the equatorial plane. These velocities reflect convective motion (to be discussed in subsection 3.5). We also notice that almost all the velocity vectors (except for some near the disk surface) are inward (i.e., towards the central black hole) at $r \lesssim 40 r_\mathrm{S}$, although a hint of convective motions is observed in snapshots (to be discussed in subsection 3.5).

3.2 Mass inflow and outflow rates

The radial profiles of the mass flow rates are a very useful tool to diagnose gas dynamics around the black hole. We calculate the following five flow rates: the mass inflow and outflow rates in the disk, the same in the outflow region (the region above the disk surface), and the net flow rate:

$$\dot{M}_\mathrm{disk}^\mathrm{in}(r) \equiv 4\pi \int_{\theta_\mathrm{surf}}^{\pi/2} d\theta \sin\theta \\ \times r^2 \rho(r,\theta) \min\{v_\mathrm{r}(r,\theta), 0\}, \tag{17}$$

$$\dot{M}_\mathrm{disk}^\mathrm{out}(r) \equiv 4\pi \int_{\theta_\mathrm{surf}}^{\pi/2} d\theta \sin\theta \\ \times r^2 \rho(r,\theta) \max\{v_\mathrm{r}(r,\theta), 0\}, \tag{18}$$

$$\dot{M}_\mathrm{outf}^\mathrm{in}(r) \equiv 4\pi \int_{0}^{\theta_\mathrm{surf}} d\theta \sin\theta \\ \times r^2 \rho(r,\theta) \min\{v_\mathrm{r}(r,\theta), 0\}, \tag{19}$$
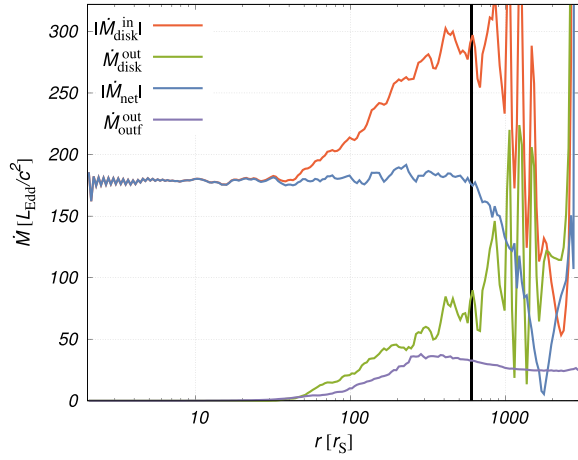
Fig. 4. Time-averaged radial profiles of the mass inflow rate, $\dot{M}_{\mathrm{disk}}^{\mathrm{in}}$ (red line), the mass outflow rate within the disk, $\dot{M}_{\mathrm{disk}}^{\mathrm{out}}$ (green line), the net flow rate, $\dot{M}_{\mathrm{net}}$ (blue line), and the mass outflow rate in the outflow region (above the disk surface), $\dot{M}_{\mathrm{outf}}^{\mathrm{out}}$ (purple line). The net flow rate is nearly constant inside the quasi-steady radius, $r_{\mathrm{qss}} \sim 600\, r_{\mathrm{S}}$, which is indicated by the vertical black line. (Color online)

$$\dot{M}_{\mathrm{outf}}^{\mathrm{out}}(r) \equiv 4\pi \int_0^{\theta_{\mathrm{surf}}} d\theta \, \sin\theta$$
$$\times r^2 \rho(r,\theta) \max\{v_{\mathrm{r}}(r,\theta), 0\}, \qquad (20)$$

$$\dot{M}_{\mathrm{net}}(r) \equiv \dot{M}_{\mathrm{disk}}^{\mathrm{in}}(r) + \dot{M}_{\mathrm{disk}}^{\mathrm{out}}(r) + \dot{M}_{\mathrm{outf}}^{\mathrm{in}}(r) + \dot{M}_{\mathrm{outf}}^{\mathrm{out}}(r). \qquad (21)$$

Here, $\theta_{\mathrm{surf}} = \theta_{\mathrm{surf}}(r)$ is the angle between the rotation axis and the disk surface (see the red line in figure 1).

Figure 4 illustrates the absolute values of the various mass flow rates as functions of radius, r, except for $\dot{M}_{\mathrm{outf}}^{\mathrm{in}}$, since it turns out to be practically zero.

Let us first focus on the blue line, which represents the net accretion rate, since this line provides key information for evaluating to what extent a quasi-steady state is achieved. We see that this line is approximately constant in the range of $r = 2\text{--}600\, r_{\mathrm{S}}$; that is, $r_{\mathrm{qss}} \equiv 600\, r_{\mathrm{S}}$. This value is unprecedentedly large (see table 1), and hence the present simulation can provide us with much more reliable information on the outflow properties.

Let us next examine the behavior of the various lines in the innermost region ($r < r_{\mathrm{inflow}} \sim 40\, r_{\mathrm{S}}$). We find negligibly small mass outflow rate (for both $\dot{M}_{\mathrm{disk}}^{\mathrm{out}}$ and $\dot{M}_{\mathrm{outf}}^{\mathrm{out}}$), while the mass inflow rate stays constant. This feature agrees well with our previous calculations (Kitaki et al. 2018). The mass inflow and outflow rates averaged over the range $r = 2\text{--}30\, r_{\mathrm{S}}$ are $\dot{M}_{\mathrm{BH}} \equiv \langle |\dot{M}_{\mathrm{disk}}^{\mathrm{in}}| \rangle = 180\, L_{\mathrm{Edd}}/c^2$, $\langle \dot{M}_{\mathrm{disk}}^{\mathrm{out}} \rangle = 4.6 \times 10^{-6}\, L_{\mathrm{Edd}}/c^2$, and $\langle \dot{M}_{\mathrm{outf}}^{\mathrm{out}} \rangle = 0.13\, L_{\mathrm{Edd}}/c^2$.

One may think that such a negligibly small mass outflow rate from the innermost region seems to be against a naive expectation that the smaller the radius, the larger the radiation-pressure force and so the larger the mass outflow rate. This is not the case, however, since the radiation flux in the comoving frame is instead inward in the innermost region because of photon trapping (see subsection 3.4). In other words, the density on the disk surface (where the radiation-pressure force balances with the gravitational force, see subsection 3.1) decreases inward so that the outflow rate ($\propto \rho v_{\mathrm{r}}$) should also decrease (see Kitaki et al. 2018).

We are now ready to examine from which part of the accretion flow the outflow emerges by examining the lines in the middle region ($40\text{--}600\, r_{\mathrm{S}}$). The outflow rate above the disk surface ($\dot{M}_{\mathrm{outf}}^{\mathrm{out}}$), indicated by the purple line in figure 4, increases with increasing radius, reaches its maximum value of $38\, L_{\mathrm{Edd}}/c^2$ at $r = 280\, r_{\mathrm{S}}(\equiv r_{\mathrm{lau}})$, and then decreases beyond. How can we understand this?

Here, we wish to stress that the outflow rate ($\dot{M}_{\mathrm{outf}}^{\mathrm{out}}$) plotted in figure 4 is cumulative. To be precise, $\dot{M}_{\mathrm{outf}}^{\mathrm{out}}(r)$ is defined by the mass flow rate measured at the radius r and so we take into account all the materials which pass through the shell at r above the disk surface, irrespective of the launching points [see equation (20)]. Therefore, the outflow rate should monotonically increase with increasing radius, as long as outflow occurs. At even larger radii ($r > 280\, r_{\mathrm{S}}$), however, $\dot{M}_{\mathrm{outf}}^{\mathrm{out}}$ decreases with increasing radius. This is because the outflowing gas which was launched at smaller radii partly goes back to the disk surface. We call this sort of outflow "failed outflow" (see the next subsection for further discussion). Note that the genuine outflow rate (by the purple line) is always less than the outflow rate in the disk (by the green line), $\dot{M}_{\mathrm{disk}}^{\mathrm{out}}$, which is caused by radial convective motion within the disk.

In the further outer region, $r \gtrsim 1000\, r_{\mathrm{s}}$, $\dot{M}_{\mathrm{outf}}^{\mathrm{out}}$ is nearly constant. The space-averaged (genuine) outflow rate at $r = 2000\text{--}3000\, r_{\mathrm{S}}$ is $\dot{M}_{\mathrm{outflow}} \equiv \langle \dot{M}_{\mathrm{outf}}^{\mathrm{out}} \rangle \sim 24\, L_{\mathrm{Edd}}/c^2$.

3.3 Outflow streamlines

Streamline analysis is a powerful tool for investigating the physical evolution of the outflowing gas after being launched from a certain point on the disk surface. Figure 5 displays a sequence of streamlines overlaid on the temperature contours. (The lower panel is a magnified view of the central region of the upper panel.) We understand in this figure that the outflow emerges from the disk surface inside the white circle at radius $r = 280\, r_{\mathrm{S}}$, where $\dot{M}_{\mathrm{outf}}^{\mathrm{out}}$ reaches its maximum (see figure 4). We define here the launching radius (R_{lau}) to be the radius where the white line crosses the red line; that is,

$$R_{\mathrm{lau}} = 280\, r_{\mathrm{S}} \sin(55°) \sim 230\, r_{\mathrm{S}} \sim 1.3 \dot{m}_{\mathrm{BH}} r_{\mathrm{S}}. \qquad (22)$$
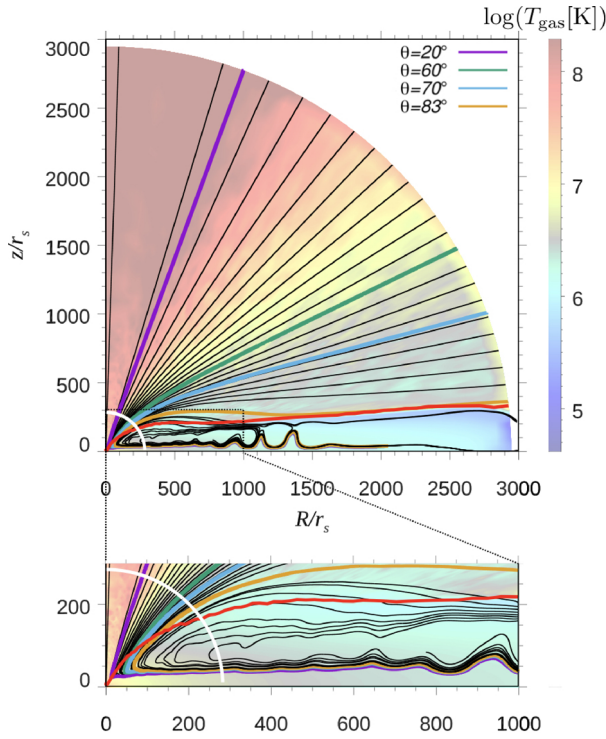
Fig. 5. Sequence of streamlines overlaid on the gas temperature contours. The upper panel is the large-scale view, while the lower panel is a magnification of the central region. In each panel we pick up several streamlines: the purple, green, light blue, and orange lines represent the streamlines which approach the lines of constant $\theta = 20°$, $60°$, $70°$, and $83°$ at $r = 3000\, r_S$, respectively. The red line indicates the disk surface, and the white line represents the loci of $r_{\mathrm{lau}} = 280\, r_S$, at which the cumulative outflow rate reaches its maximum. (Color online)

This value is consistent with the analytical estimation [equation (3)].

The streamlines between the orange and red lines in figure 5 represent the failed outflow; that is, the outflow which first leaves the disk surface at smaller radii but eventually comes back to the disk at large radii. The launching radius of the genuine outflow (which can reach the outer boundary of the computational box) is given by

$$R_{\mathrm{lau}}^{\infty} = 190\, r_S \sin(46°) \sim 140\, r_S \sim 0.75 \dot{m}_{\mathrm{BH}} r_S. \qquad (23)$$

The Bernoulli parameter, Be, is everywhere negative in the failed outflow region, and in the pure outflow region around the disk surface. We should note, however, that the Bernoulli parameter is not a conserved quantity in the viscous flow, and that Be is positive far from the black hole in the pure outflow region.

It is interesting to examine how the physical quantities vary along each streamline. Figure 6 illustrates the variations of the physical quantities along each of the colored streamlines depicted in figure 5. We consider first the purple solid line (this streamline is connected to the funnel region, see figure 5). From the middle panel we understand that the
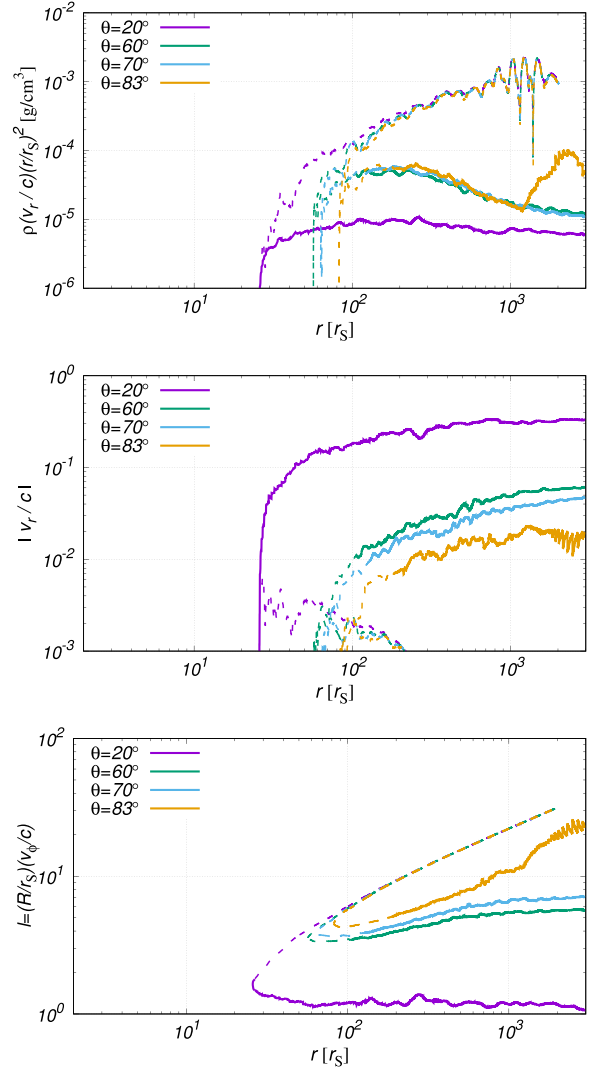

Fig. 6. Variations of some physical quantities along the four colored streamlines shown in figure 5: the mass flow rates per unit solid angle (top), the absolute values of the radial velocity (middle), and the specific angular momenta (bottom). The solid (dashed) lines indicate the quantities in the outflow (disk) region. (Color online)

gas is quickly accelerated to finally acquire a high velocity, $v_r \sim 0.3\, c$, within the funnel. The outflow rate ($r^2 \rho v_r \sim$ const) is conserved along the streamline within the funnel (see the upper panel). Thus, the radial profile of the gas mass density is roughly $\rho \propto r^{-2}$. The specific angular momentum ($R v_\phi$) is also conserved (see the lower panel). This can be easily understood, since the viscosity is not effective in the outflow region.

Let us next consider the green and light blue lines, both of which are connected to the (genuine) outflow region in figure 6. From the middle panel, we see that the radial velocities are gradually accelerated until they reach the final value of several tenths of c at around $r \gtrsim 10^3\, r_S$. Again,
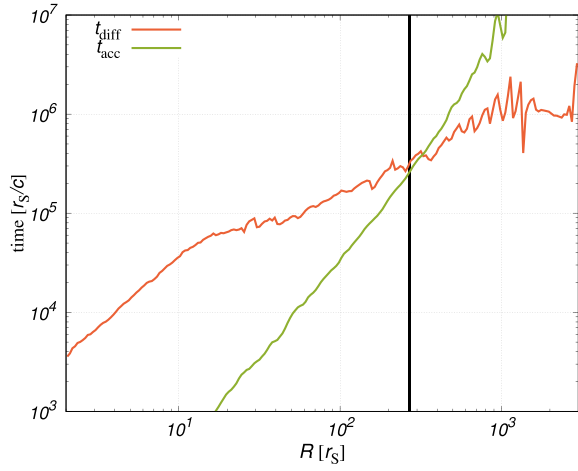
Fig. 7. Radiative diffusion timescale (red) and timescale (green), both evaluated on the equatorial plane. The vertical black line is the photon-trapping radius calculated based on the slim-disk model ($R_{trap} \sim 270\,r_S$). (Color online)
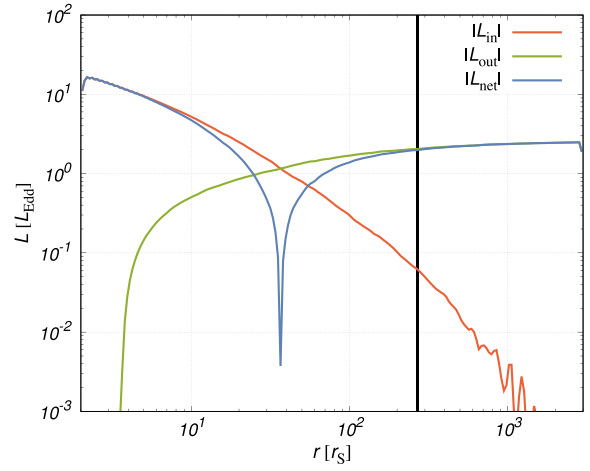

Fig. 8. Radial profiles of the inward, outward, and net luminosities. The vertical black line indicates the photon-trapping radius based on the slim-disk model ($R_{trap} \sim 270\,r_S$). (Color online)

the specific angular momenta are roughly conserved, as is shown in the bottom panel.

The orange solid line in each panel of figure 6 shows similar tendencies to the green and light blue solid lines, except in the region around $r \sim 3000\,r_S$, where the outflowing gas comes back to the disk surface region and merges there.

3.4 Photon-trapping radius

The principal value characterizing the super-Eddington accretion disk is the photon-trapping radius [see equation (2)]. The photon-trapping radius is the radius where the radiative diffusion timescale t_{diff} is equal to the dynamical timescale t_{dyn}, where

$$t_{diff} = \frac{H_{inf}(R)}{c/[3\tau_e(R)]}, \tag{24}$$

$$t_{dyn} = \frac{R}{|v_r(R, z=0)|}. \tag{25}$$

Here, H_{inf} is the height under which the radial velocity is negative, and τ_e is the vertical Thomson optical depth measured from the equatorial plane to $z = H_{inf}(R)$. Figure 7 shows these two timescales, and they intersect at $R_{trap} \sim 330\,r_S$. By contrast, the photon-trapping radius which the slim-disk model predicts is $R_{trap} \sim 270\,r_S$ [see equation (2)]. This value is close to the one estimated numerically in the present study.

We evaluate the photon-trapping radius from another viewpoint. The inward, outward, and net luminosities are, respectively, written as

$$L_{in}(r) = \int_{4\pi} d\Omega\, r^2 \min\left\{F_{lab}^r, 0\right\}, \tag{26}$$

$$L_{out}(r) = \int_{4\pi} d\Omega\, r^2 \max\left\{F_{lab}^r, 0\right\}, \tag{27}$$

and

$$L_{net}(r) = L_{in}(r) + L_{out}(r). \tag{28}$$

Here, F_{lab}^r is the radial component of radiation flux in the laboratory frame. In figure 8 we compare these luminosities. The inward luminosity, which represents the photon-trapping effect, increases inward, and the two lines intersect at $r \sim 38\,r_S$, which is significantly less than the photon-trapping radius derived based on the slim-disk model; i.e., $R_{trap} \sim 270\,r_S$. If we take the radius where $L_{in}(r)$ vanishes, it is $\sim 10^3\,r_S$, much larger than R_{trap}.

Why are these estimations so distinct? We should note here that the diffusion timescale depends on the vertical position of the region in question; the larger the vertical position (z), the shorter the diffusion timescale. We thus undertook further analysis; namely, we continuously connect the radiation flux vectors starting from the disk surface, as we did in the streamline analysis to follow gas motion, and display the resultant "flux-line" in figure 9. (Note that this flux-line does not have the same meaning as streamlines, since the divergence of the radiation flux is not zero, and since photons diffuse as they proceed inward.) We see that the flux-lines starting from the disk surface at $R < 450\,r_S \sim 2.5\,\dot{m}_{BH}r_S$ are eventually connected to the black hole region. We thus take this value as the numerical trapping radius, which is close to the analytical estimation.

The previous GR-RMHD simulations revealed that the magnetic fields help the photons to escape from the disk surface, since the gas moves towards the disk surface by magnetic buoyancy and the photons are trapped in the gas
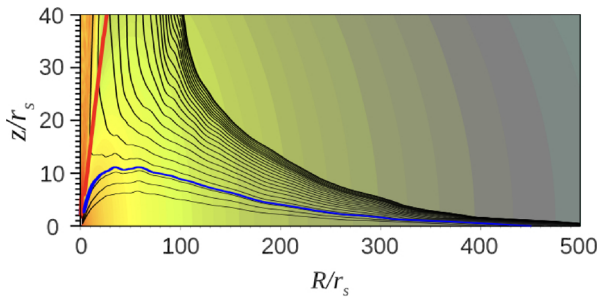
Fig. 9. Radiation flux-line (black lines) overlaid on the gas temperature contours (figure 2). The red line indicates the disk surface. The blue line starts at $R \sim 450\, r_S$ on the equatorial plane and is connected to the black hole because of the photon-trapping effect. (Color online)

(e.g., Blaes et al. 2011; Jiang et al. 2019). Therefore, the photon-trapping radius may become smaller in GR-RMHD simulations.

3.5 Convection in the accretion disk

It is well known that the super-Eddington accretion flow undergoes large-scale circular gas motion or convection (see, e.g., Eggum et al. 1988). Since the entropy generated within the accretion disk cannot easily be taken away from the disk because of the inefficient radiative diffusion in the vertical direction, the entropy tends to increase as gas accretes, a condition for convective instability, as in the case of radiatively inefficient flow (see, e.g., Narayan & Yi 1994).

Pietrini and Krolik (2000) proved that convection in which the vertical wavelength is larger than the radial wavelength occurs in the radiation-pressure-dominated disk by deriving the dispersion relation from the RHD equations. Some analytical and semi-analytical studies were produced to describe the vertical structure under the assumption of separating the radial and vertical structures. For example, Sądowski et al. (2011) calculated the vertical structure of the super-Eddington accretion disk by the Runge–Kutta method, and showed that the energy is transported in a vertical direction by the convection, while Gu (2012) derived a self-similar solution of the super-Eddington accretion disk by assuming radial dependence of the gas mass density and the radiation energy density, and this solution does not satisfy the convection criterion. Thus, the occurrence of convection is a controversial issue and the previous studies may depend on the various assumptions for splitting the radial and vertical structure.

To proceed, it is useful to perform numerical simulations. It seems important to note that convection also occurs in the inner region of the standard disk, where radiation pressure is dominant. This is because the radiation
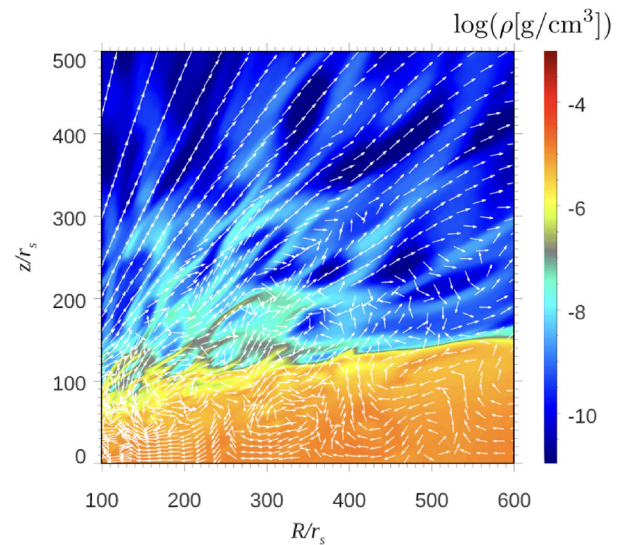

Fig. 10. Snapshot of the density contours overlaid with velocity vectors in the region $100\, r_S \le R \le 600\, r_S$. We clearly see convection cells in the disk. (Color online)
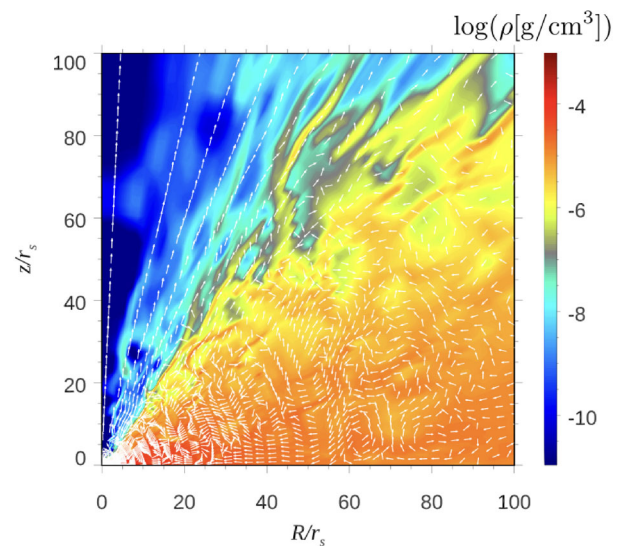

Fig. 11. As figure 10 but in the central region near the black hole. We see convective cells even in the vicinity of the black hole at $r < r_{inflow} \sim 40\, r_S$, which were not visible in the time-averaged profile (see figure 3). (Color online)

diffusion becomes inefficient, as in the case of the super-Eddington accretion flow. According to the RHD simulations of the standard disk, the energy in the radiation-pressure-dominated region is transported not by radiation diffusion but by advection of the radiation (Agol et al. 2001; Blaes et al. 2011). Considering these studies of the standard disk, we conclude that analyzing the energy budget is very useful in evaluating the convection in the super-Eddington accretion disk.

As mentioned in subsection 3.2, convection occurs in the super-Eddington accretion disk. Figures 10 and 11 show

snapshots of the cross-sectional view of the accretion flow. We see there circular motions of velocity vectors around several points, e.g., $(R, z) = (17\,r_S, 10\,r_S)$, $(50\,r_S, 20\,r_S)$, $(320\,r_S, 50\,r_S)$, and $(470\,r_S, 110\,r_S)$. These convections tend to rotate in the clockwise direction. This is because the radiation force and the centrifugal force tend to overcome the gravitational force when the gas blob rises from the equatorial plane to the surface of the disk.

It is very important, however, to note that small-scale convective motions totally disappear and global convection appears when we make a time average (see figures 1 and 2). Here, we wish to emphasize that this global convective motion is constructed by time-averaging the small-scale circular motions. The time-averaged direction of the gas motion is inward near the equatorial plane, while it is outward near the surface of the accretion disk. The inflow and outflow motions in the disk by global convection are dominant over the entire accretion flow (see the red and green lines in comparison with the purple line in figure 4).

It was previously indicated that the occurrence of convection in snapshots may depend on the adopted α-parameter; smaller α means more efficient convection motion (Igumenshchev & Abramowicz 1999, 2000; Yang et al. 2014), and the α-parameter decreases with increasing radius ($\alpha \sim 0.05$–0.2; Jiang et al. 2019). Therefore, the (time-averaged) global convection may be modified if we adopt smaller α-parameter values and/or if we perform RMHD simulations.

3.6 Energy transportation by convective motion

Plotting the heating and cooling rates is a powerful tool for diagnosing gas dynamics in the disk, as demonstrated by Blaes et al. (2011). In the gas energy equation, viscous heating and advective heating balance with the energy transported to the radiation,

$$\Phi_{\mathrm{vis}} + q_{\mathrm{gas}}^{\mathrm{adv}} = \Gamma_{\mathrm{comp}} + (4\pi\kappa B - c\kappa E_0), \qquad (29)$$

while in the radiation energy equation, energy transported from the gas balances with the radiation advection cooling and radiative diffusion,

$$\Gamma_{\mathrm{comp}} + (4\pi\kappa B - c\kappa E_0) = q_{\mathrm{rad}}^{\mathrm{adv}} + q_{\mathrm{rad}}^{\mathrm{diff}}. \qquad (30)$$

The terms in this equation are defined as

$$q_{\mathrm{gas}}^{\mathrm{adv}} \equiv -\left[\nabla \cdot (e\boldsymbol{v}) + p\nabla \cdot \boldsymbol{v}\right], \qquad (31)$$

$$q_{\mathrm{rad}}^{\mathrm{adv}} \equiv \nabla \cdot (E_0\boldsymbol{v}) + \nabla\boldsymbol{v} : \mathbf{P}_0, \qquad (32)$$

$$q_{\mathrm{rad}}^{\mathrm{diff}} \equiv \nabla \cdot \boldsymbol{F}_0. \qquad (33)$$
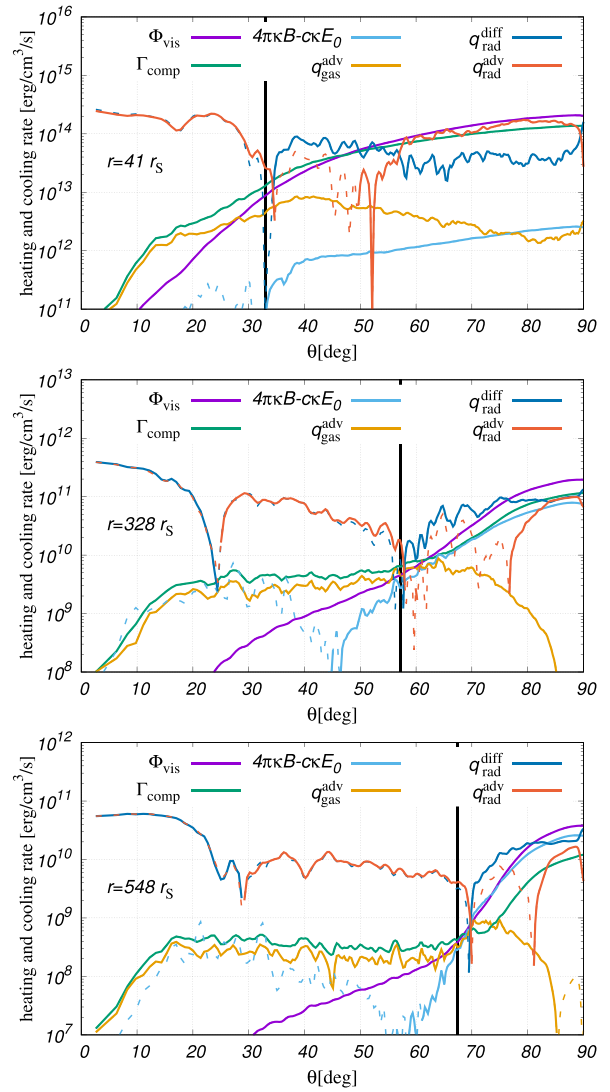

Fig. 12. Polar angle dependencies of the heating and cooling rates at three different radii: $r = 41\,r_S$ (top), $r = 328\,r_S$ (middle), and $r = 548\,r_S$ (bottom). The colored lines represent the following quantities: the viscous heating (purple), the net radiation heating and cooling (light blue), the advection of the radiation (red), the Compton heating and cooling (green), the advection of the gas (orange), and the radiation diffusion (blue). The black vertical line indicates the polar angle of the disk surface (see figure 1). The solid lines mean that each value is positive (e.g., $4\pi\kappa B - c\kappa E_0 > 0$), whereas the dashed lines mean that each value is negative (e.g., $4\pi\kappa B - c\kappa E_0 < 0$). (Color online)

Here, Φ_{vis} is the viscous heating, $q_{\mathrm{gas}}^{\mathrm{adv}}$ is the advection of the gas, including work by the gas pressure, Γ_{comp} is the Compton heating and cooling, $(4\pi\kappa B - c\kappa E_0)$ is the net heating rate due to emission and absorption of radiation, $q_{\mathrm{rad}}^{\mathrm{adv}}$ is the advection of the radiation, including work by the radiation pressure, and $q_{\mathrm{rad}}^{\mathrm{diff}}$ is the radiation diffusion.

Figure 12 shows the angle dependencies of these heating and cooling rates at each radius. We numerically confirmed that equations (29) and (30) roughly hold. See also table 2 for a summary of the dominant terms.

Table 2. Dominant heating and cooling rate.*

Region	Angle (θ)		Radius (r)	Gas energy equation heating/cooling	Radiation energy equation heating/cooling
Equatorial plane	$(\sim 90^\circ)$	Inner part	$(r \lesssim 330\,r_\mathrm{S})$	$\Phi_\mathrm{vis} \sim \Gamma_\mathrm{comp}$	$\Gamma_\mathrm{comp} \sim q_\mathrm{rad}^\mathrm{adv}$
		Middle part	$(330\,r_\mathrm{S} \lesssim r \lesssim r_\mathrm{qss})$	$\Phi_\mathrm{vis} \sim (4\pi\kappa B - c\kappa E_0)$	$(4\pi\kappa B - c\kappa E_0) \sim q_\mathrm{rad}^\mathrm{diff}$
Disk surface	$(\sim \theta_\mathrm{surf})$		$(r \lesssim r_\mathrm{qss})$	$\Phi_\mathrm{vis} + q_\mathrm{gas}^\mathrm{adv} \sim \Gamma_\mathrm{comp}$	$\Gamma_\mathrm{comp} \sim q_\mathrm{rad}^\mathrm{adv} + q_\mathrm{rad}^\mathrm{diff}$

*The dominant heating and cooling rate in gas and radiation energy equations at each spatial point [see equations (29) and (30)].

It is important to note that it is not advective cooling but advective heating that works in the gas energy equation. The reason for this can be understood in the following way (Nakamura et al. 1997). Entropy is generated via viscous dissipation within the gas so that the gas is heated, but the internal energy is quickly transported to the radiation via the Compton process. This results in a monotonic decrease of the gas entropy towards the center. Since the higher-entropy gas moves inwards, the advection works as heating.

The dominant terms in equations (29) and (30) vary at each spatial position and are shown in table 2. When we focus near the equatorial plane ($\theta \sim 90^\circ$) in figure 12, the viscous heating is much larger than the advection of the gas ($\Phi_\mathrm{vis} \gg q_\mathrm{gas}^\mathrm{adv}$). The energy is transported from gas to radiation by the Compton effect near the black hole, whereas it is transported by the net radiation heating and cooling far from the black hole. The advection of the radiation is dominant near the black hole, but the radiation diffusion is dominant far from the black hole. Hence, the energy balance near the equatorial plane is roughly $\Phi_\mathrm{vis} \sim \Gamma_\mathrm{comp} \sim q_\mathrm{rad}^\mathrm{adv}$ near the black hole, and $\Phi_\mathrm{vis} \sim (4\pi\kappa B - c\kappa E_0) \sim q_\mathrm{rad}^\mathrm{diff}$ far from the black hole.

Let us next consider the region just below the disk surface. We then see that in figure 12, the viscous heating is comparable to advection of the gas ($\Phi_\mathrm{vis} \sim q_\mathrm{gas}^\mathrm{adv}$). The energy is transported from gas to radiation by the Compton effect. The advection of the radiation is comparable to the radiation diffusion. The relation of equations (29) and (30) near the photosphere is roughly $\Phi_\mathrm{vis} + q_\mathrm{gas}^\mathrm{adv} \sim \Gamma_\mathrm{comp} \sim q_\mathrm{rad}^\mathrm{adv} + q_\mathrm{rad}^\mathrm{diff}$.

The energy is carried by the advection of the radiation in a vertical direction near the black hole ($R \lesssim R_\mathrm{trap} \sim 330\,r_\mathrm{S}$). This process corresponds to energy transportation by convection. We confirmed that the advection term, $\nabla \cdot (E_0 \boldsymbol{v})$, is larger than the work by radiation pressure, $\nabla \boldsymbol{v} : \mathbf{P}_0$, by a factor of several [i.e., $q_\mathrm{rad}^\mathrm{adv} \sim \nabla \cdot (E_0 \boldsymbol{v})$]. The advection term, $\nabla \cdot (E_0 \boldsymbol{v})$, has radial and angular components, and these components are approximately comparable to each other. The radiation energy is carried by $E_0 \boldsymbol{v}$ in the vertical direction. In other words, the radiation energy moves with the gas.

We understand that the radiation is trapped in teh gas by Lorentz transformation of the radiation flux (Ohsuga & Mineshige 2007). The formula in the optically thick region is written as

$$F_\mathrm{lab}^i = F_0^i + v^i E_0 + v_j \mathrm{P}_0^{ij} \propto v^i E_0, \tag{34}$$

where F_lab^i is the radiation flux in the laboratory frame. The comoving flux in the optically thick region is represented by the diffusion approximation, $\boldsymbol{F}_0 = -c\nabla E_0/(3\rho\kappa)$, and we assume that the radiation diffusion is inefficient, $F_0^i \ll v^i E_0$ (i.e., the photon-trapping effect). The third term on the right-hand side of equation (34), $v_j \mathrm{P}_0^{ij}$, is equal to $E_0 v^i/3$, and corresponds to the work by the radiation pressure (Mihalas & Mihalas 1984). From these relations, we understand that $F_\mathrm{lab}^i \sim v^i E_0$ is established in the super-Eddington accretion disk, and this formula means that the radiation moves with the gas. In particular, energy is transported inward with the gas velocity, but the energy carrier is the radiation under the radiation-pressure-dominant region.

4 Discussion

4.1 Comparison with the super-Eddington accretion model in Kitaki et al. (2018)

Kitaki et al. (2018) performed rather extensive parameter studies of RHD simulations of the super-Eddington accretion flow and derived semi-analytical formulas for representative physical quantities of the disk (e.g., temperature, density, radial velocity, and so on) as functions of black hole mass, accretion rate, and radius. Figure 13 shows the ratios of the present numerical values to those reported by Kitaki et al. (2018). We focus on the range $r \lesssim 600\,r_\mathrm{S}$, where the quasi-steady state is achieved (see subsection 3.2). The present numerical results, except for gas mass density, agree well with those of Kitaki et al. (2018) within a factor of 2.

For the gas mass density we find reasonable agreement in the inner region ($r \lesssim 200\,r_\mathrm{S}$), but we notice significant discrepancies at larger radii. The reason for the discrepancies can be understood in relation to the fact that the mass outflow rate is comparable to the (net) inflow rate there. In fact,
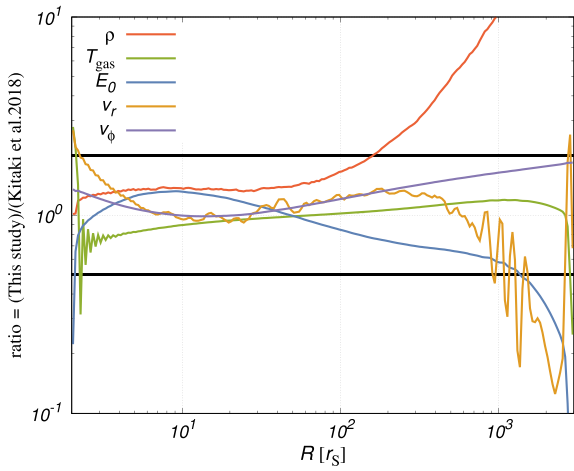
Fig. 13. Ratios of the values of some physical quantities (density, temperature, etc.) obtained by the present simulation to those derived by the formulas of Kitaki et al. (2018). The following values are inserted into the formulas: $M_{BH} = 10 M_\odot$, $\dot{M}_{BH} = 180 L_{Edd}/c^2$, and $\alpha = 0.1$. The colored lines represent the gas mass density (red), the gas temperature (green), the radiation energy density (blue), the radial velocity (orange), and the azimuthal velocity (purple). The results agree well (except for the density at large radii) within a factor of 2 in the region sandwiched by the two horizontal black lines. (Color online)

the inflow and outflow rates increase outward at $r \gtrsim 200\, r_S$ (see figure 4). The formulas by Kitaki et al. (2018) were derived in the regime in which outflow is negligible compared with inflow. Although the density profile shows some discrepancies, the radial velocity profile does not, since the latter is rather insensitive to $\dot{M}_{BH}$ (Watarai 2006; Kitaki et al. 2018). In conclusion, we are not allowed to apply the formulas to the present numerical results in the region $r \gtrsim 200\, r_S$ where the outflow is substantial.

As future work it will be useful to derive new formulas describing the accretion disk structure in the regime in which the outflow rate is comparable to the inflow rate.

4.2 Impact on the environment

As we stressed in section 1, the impact on the environment seems to have been grossly overestimated in the previous simulation studies, since the outflow was mostly launched from the initial Keplerian torus. In our simulation we can give more realistic estimations of the impact of the outflow.

Figure 14 shows the θ profiles of the mass flux, the momentum fluxes, and the energy fluxes measured at $r = 2545\, r_S$ multiplied by r^2 in the upper to lower panels, respectively. (In other words, $d\dot{M}/d\Omega$, $d\dot{J}_i/d\Omega$ with $i = r, \theta$, and ϕ, and $d\dot{E}/d\Omega$ are plotted, where $\dot{J}_i$ is the momentum flow rate, and $\dot{E}$ is the energy flow rate.) The energy fluxes
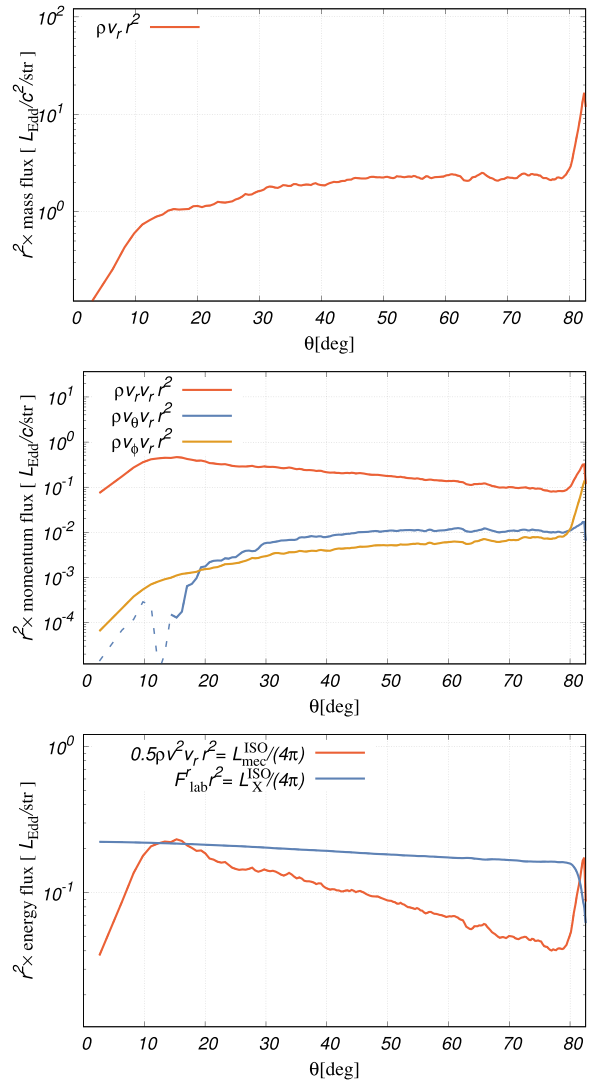

Fig. 14. Angular profile of the mass fluxes (top), the momentum fluxes (middle), and the energy fluxes (bottom) at $r = 2545\, r_S$ in the range $\theta = 0°$ –$83°$ ($= \theta_{surf}$). The solid lines mean that each value is positive (e.g., $0 < \rho v_\theta v_r \propto v_\theta$), and the dashed lines mean that each value is negative (e.g., $0 > \rho v_\theta v_r \propto v_\theta$). (Color online)

are also connected to the isotropic X-ray luminosity and the isotropic mechanical luminosity calculated by

$$L_X^{ISO}(\theta) = 4\pi r^2 F_{lab}^r, \tag{35}$$

$$L_{mec}^{ISO}(\theta) = 2\pi r^2 \rho v^2 v_r. \tag{36}$$

Here, $v^2 = v_r^2 + v_\theta^2 + v_\phi^2$ is the total gas velocity, and we assume that radiation is emitted predominantly in the X-ray band, since the ratio between the X-ray luminosity and the bolometric luminosity is ~71%–98% (Kitaki et al. 2017; Narayan et al. 2017).

We notice that the radiation luminosity has a peak in the face-on ($\theta = 0$) direction, while the mass outflow rate increases towards the edge-on direction, and the

momentum flux and the mechanical luminosity reach their maximum at $\theta \sim 15°$. In the inner funnel region (with $\theta \sim 0°$–$15°$), all the lines except for the radiative flux rapidly decrease with a decrease in θ. This is because the gas mass density rapidly decreases inward (towards the rotation axis). Although the radial velocity increases towards the rotation axis, the change in ρ overcomes that in v_r so that ρv_r decreases with decreasing θ.

In the outflow region ($\theta \sim 20°$–$83°$), by contrast, the radial components of the fluxes (ρv_r, ρv_r^2, $0.5 \rho v^2 v_r$) only slightly or scarcely change in the polar direction.

The isotropic X-ray luminosity decreases slightly with increasing angle by less than a factor of 2. The previous studies showed, however, that the isotropic X-ray luminosity varies by a factor of ~ 10 in the azimuthal direction (e.g., Ogawa et al. 2017). This difference stems from the different outflow properties. That is, a much larger amount of gas is blown away in the previous studies because of the small value of the Keplerian radius adopted. It is difficult for photons generated inside the disk region (with small θ) to pass through the outflow region (at large θ).

Observational determination of the inclination angle seems to be difficult. By contrast, the spectral shape is sensitive to the inclination angle because of the significant Compton scattering within the outflow region (Kawashima et al. 2012). Spectral calculation based on our hydrodynamic simulation data is left as future work.

4.3 The energy conversion

The energy conversion efficiency is one of the key quantities in accretion problems. In subsection 3.2, we evaluated the inflow rate at the black hole as $\dot{M}_{\mathrm{BH}} \sim 180\,L_{\mathrm{Edd}}/c^2$, and the outflow rate above the surface of the disk at around r_{out} as $\dot{M}_{\mathrm{outflow}} \sim 24\,L_{\mathrm{Edd}}/c^2$. We should note that the numerical results in $r \geq r_{\mathrm{qss}} = 600\,r_{\mathrm{S}}$ are not so reliable, since the quasi-steady assumption does not hold there. But we can accurately estimate the outflow quantities, such as the outflow rate $\dot{M}_{\mathrm{outflow}}$ at r_{out}, since the outflows are launched at relatively small radii, i.e., $r_{\mathrm{lau}} \sim 280\,r_{\mathrm{S}} < r_{\mathrm{qss}}$. The inflow and outflow conversion efficiencies are calculated as

$$\beta \equiv \frac{\dot{M}_{\mathrm{outflow}}}{\dot{M}_{\mathrm{BH}}} \sim 0.14, \tag{37}$$

$$\beta_{\mathrm{in}} \equiv \frac{\dot{M}_{\mathrm{BH}}}{\dot{M}_{\mathrm{BH}} + \dot{M}_{\mathrm{outflow}}} \sim 0.88, \tag{38}$$

$$\beta_{\mathrm{out}} \equiv \frac{\dot{M}_{\mathrm{outflow}}}{\dot{M}_{\mathrm{BH}} + \dot{M}_{\mathrm{outflow}}} \sim 0.12. \tag{39}$$

Here, the denominators of equations (38) and (39), $\dot{M}_{\mathrm{BH}} + \dot{M}_{\mathrm{outflow}}$, mean the injected mass flow rate from the surrounding environment under the assumption that the net flow rate is entirely constant in radius. Hence, we conclude that about 12% of the injected gas turns into outflow.

The luminosity measured by a distant observer is calculated by

$$L_{\mathrm{X}} \equiv 4\pi \int_0^{\theta_{\mathrm{surf}}} d\theta \sin\theta\, r^2 \max\left\{F_{\mathrm{lab}}^r, 0\right\}, \tag{40}$$

and is $L_{\mathrm{X}} \sim 2.5\,L_{\mathrm{Edd}}$ at $r = 2545\,r_{\mathrm{S}}$ (near the outer boundary), while the predicted luminosity from the slim-disk formula is given by (Watarai et al. 2001)

$$L_{\mathrm{slim}} = \left[1 + \ln\left(\frac{1}{30}\frac{\dot{M}_{\mathrm{BH}}}{L_{\mathrm{Edd}}/c^2}\right)\right] L_{\mathrm{Edd}} \sim 2.8\,L_{\mathrm{Edd}}, \tag{41}$$

and is in reasonable agreement.

The mechanical luminosity of the outflow is given by

$$L_{\mathrm{mec}} \equiv 4\pi \int_0^{\theta_{\mathrm{surf}}} d\theta \sin\theta\, r^2 \max\left\{\frac{1}{2}\rho v^2 v_r, 0\right\}, \tag{42}$$

and is $L_{\mathrm{mec}} \sim 0.16\,L_{\mathrm{Edd}}$ at $r = 2545\,r_{\mathrm{S}}$ (near the outer boundary). The ratio of the luminosities is $L_{\mathrm{mec}}/L_{\mathrm{X}} \sim 0.07$. Hence, the energy carried outside by the radiation is larger than that by the outflow.

4.4 Outflow in ULXs

Some ULXs are accompanied by optical nebulae with extents of 10–100 parsecs (e.g., Kaaret et al. 2004) and/or radio bubbles with extents of 10–100 parsecs (e.g., Berghea et al. 2020). These nebulae are thought to originate from the outflow in super-Eddington accretion flow. The isotropic X-ray luminosities of the central object and the mechanical luminosities of the outflow are listed in table 3 for some ULXs. On the observational side, the isotropic X-ray luminosities are evaluated from the photons which come directly to the observer, and the mechanical luminosities are evaluated from the optical radiation. The values of $L_{\mathrm{X}}^{\mathrm{ISO}}$ and L_{mec} evaluated in the present study are thus consistent with the observed luminosities in ULXs (see table 3).

We wish also to note that the iron absorption lines in X-ray with Doppler velocities of $\sim 0.2\,c$ are discovered by stacking analysis (Pinto et al. 2016), and these velocities are consistent with our results.

4.5 Future issues

The M-1 closure method, an alternative method for calculating radiation flux, etc., is extensively used in recent simulations instead of the flux-limited diffusion (FLD) method (e.g., Sądowski et al. 2015). We note, however, that there

Table 3. The X-ray luminosities and the mechanical luminosities.*

Object	L_X^{ISO} [10^{39} erg s^{-1}]	L_{mec} [10^{39} erg s^{-1}]	$L_{\mathrm{mec}}/L_X^{\mathrm{ISO}}$
Our simulation ($\theta = 2.°6$–$80°$)	$\sim$2.6–3.7	$\sim$0.20	$\sim$0.05–0.08
Holmberg II X-1 (ULX)	$\sim$5–16[†]	$\sim$0.7[‡]	$\sim$0.04–0.14
IC 342 X-1 (ULX)	$\sim$10–20[§]	$\sim$3[‡]	$\sim$0.15–0.3

*Here, L_X^{ISO} is the isotropic X-ray luminosity of a central object, and L_{mec} is the mechanical luminosity of the outflow.

[†]Kaaret, Ward, and Zezas (2004).

[‡]Abolmasov et al. (2007).

[§]Shidatsu, Ueda, and Fabrika (2017).

[‖]Fürst et al. (2016).

[♯]Pakull, Soria, and Motch (2010).

will be practically no big differences in the calculated accretion disk structure between them, since both methods give the correct formula of the radiative diffusion approximation in the optically thick regime. In the optically thin region (e.g., the outflow region), by contrast, we find slight differences, since the M-1 closure gives a different solution compared with the FLD method there (e.g., in the beam problem, the shadow test, etc.; see González et al. 2007). Further, we wish to point out that the M-1 closure method does not always give the correct radiation fields, since the M-1 closure method is also an approximation and it is known to produce inaccurate results in nonuniform radiation fields; see, e.g., Ohsuga and Takahashi (2016) for the case of a radiation hydrodynamic shock. This issue will only be resolved by full-transfer simulations in the future.

We assume equatorial symmetry in our simulation. When we expand the simulation box in the polar direction from $\theta = 0$–$\pi/2$ to $\theta = 0$–π, the flow pattern in the disk may be slightly modified by the convective motion across the equatorial plane, which is seen in Sądowski and Narayan (2016), but it is hard to believe that the disk structure will change dramatically from our results.

The next issue is three-dimensional simulations. Sądowski and Narayan (2016) compared the results of 2D and 3D GR-RMHD simulations of the super-Eddington accretion flow, and reported that the physical values in the accretion disk (e.g., rotational velocity, surface density) are almost the same within an error of 10%. They also showed that the radiation energy density differs only within a factor of 2 between 2D and 3D simulations. We thus believe that there will be no significant differences, as far as the global structure is concerned, but 3D simulations are definitely needed in future for more advanced study, e.g., spatiotemporal variation studies.

We used the α prescription for simplicity (Shakura & Sunyaev 1973), although magnetorotational instability is believed to be one of the most plausible origins of the

viscosity (Balbus & Hawley 1991, 1992). Sądowski et al. (2015) calculated the super-Eddington accretion flow by GR-RMHD simulation and found that the viscosity parameter is $\alpha \sim 0.1$ and is roughly constant in the radius outside the innermost stable circular orbit. Therefore, we conclude that our assumption ($\alpha = 0.1$) is reasonable, but in future we need full radiation-MHD simulations for confirmation.

5 Concluding remarks

In the present study we have carefully solved the structure of the super-Eddington accretion flow and associated outflow, and examined from where in the accretion flow the outflow is launched and how much material, momentum, and energy can be blown away to a large distance. For this purpose, we greatly expanded the simulation box to $r_{\mathrm{out}} = 3000\,r_S$ and set an extremely large initial Keplarian radius, $r_K = 2430\,r_S$, compared with the previous studies. We could, hence, achieve an unprecedentedly large quasi-steady radius, $r \leq r_{\mathrm{qss}} \sim 600\,r_S$, within which a quasi-steady state is realized.

In figure 15 we summarize our view of the structure of the super-Eddington accretion flow and associated outflow obtained through the present study. In this figure we plot gas motion (both circular motion within the disk and outflow from the disk surface). The main features can be summarized as follows:

- The disk thickness (H) is roughly proportional to R (i.e., $H/R \sim 1$) near the black hole, whereas it is constant in radius, $H \sim (2$–$3) \times 10^2\,r_S \sim (1.1$–$1.7)\dot{m}_{\mathrm{BH}}r_S$, far from the black hole. The photon-trapping radius, $R_{\mathrm{trap}} \sim 450\,r_S \sim 2.5\,\dot{m}_{\mathrm{BH}}r_S$, approximately separates these two regions. This feature is consistent with the prediction of the slim-disk model and the standard Shakura–Sunyaev disk.
- From the streamline analysis we find that the gas on the disk surface at $R \leq R_{\mathrm{lau}} \sim 230\,r_S \sim 1.3\,\dot{m}_{\mathrm{BH}}r_S$ is blown
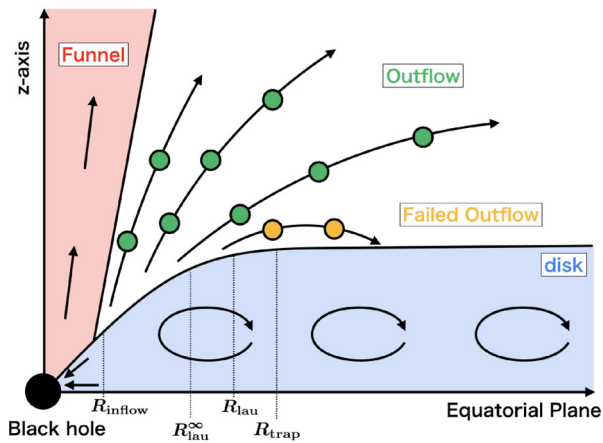
Fig. 15. Schematic view of the structure of the super-Eddington accretion flow and associated outflow based on our numerical results. The black arrows indicate the gas motion. (Color online)

away to produce outflow (see figure 5). The genuine outflow (which reaches the outer calculation boundary) is launched at $R \lesssim R_{\mathrm{lau}}^{\infty} \sim 140\,r_{\mathrm{S}} \sim 0.75\,\dot{m}_{\mathrm{BH}}r_{\mathrm{S}}$, well inside the trapping radius, while the failed outflow originates from the region between $R \sim R_{\mathrm{lau}}^{\infty}$ and R_{lau} (see figure 5). Systematic simulation studies to confirm the $\dot{m}_{\mathrm{BH}}$ dependencies of these radii (e.g., R_{lau}) are left as future work.

- The black hole accretion rate in our study is $\dot{M}_{\mathrm{BH}} \sim 180\,L_{\mathrm{Edd}}/c^2$ and the outflow rate is $\dot{M}_{\mathrm{outflow}} \sim 24\,L_{\mathrm{Edd}}/c^2$. The ratio of the isotropic X-ray luminosity to the mechanical luminosity is $L_{\mathrm{mec}}/L_{\mathrm{X}}^{\mathrm{ISO}} \sim 0.05$–$0.08$, which is consistent with observations of ULXs surrounded by optical nebulae.

- We separately examined the energy balance for the radiation and for the gas. Around the equatorial plane, the gas is heated via viscous dissipation and is cooled by emitting radiation at large radii, as formulated in the standard disk model, but is cooled by inverse Compton scattering at small radii. The radiation is heated through inverse Compton scattering and is cooled by advection of the radiation at small radii, as formulated in the slim-disk model. The situation is somewhat different near the disk surface, where gas is heated both by viscous dissipation and advective heating (not cooling), which occurs since the entropy decreases inward as gas accretes as a consequence of significant Compton cooling.

- Convection (or large-scale circulation) occurs over nearly all the accretion disk. Convective motions are observed even inside $R_{\mathrm{inflow}} \sim 40\,r_{\mathrm{S}} \sim 0.22\,\dot{m}_{\mathrm{BH}}r_{\mathrm{S}}$ in snapshots (see figure 11), although they are smeared out when time-averaged (see figure 3). The direction of the convective motion is sometimes clockwise and sometimes anti-clockwise, but more frequently we see clockwise motion, when we set the black hole at the lower-left corner (see figures 10 and 11).

- Most of the previous simulation studies show a puffed-up structure near the black hole ($R \ll R_{\mathrm{trap}}$), which seems to be formed as a direct consequence of adopting a very small Keplerian radius. We caution that a large amount of mass outflow can be produced by such a puffed-up structure, and that cases with small Keplarian radii may be applied to the tidal disruption events which undergo super-Eddington accretion. This is because the objects disrupted by tidal action came close to the black hole.

Acknowledgments

References

Abolmasov, P., Fabrika, S., Sholukhova, O., & Afanasiev, V. 2007, Astrophysical Bull., 62, 36

Abramowicz, M. A., Czerny, B., Lasota, J. P., & Szuszkiewicz, E. 1988, ApJ, 332, 646

Agol, E., Krolik, J., Turner, N. J., & Stone, J. M. 2001, ApJ, 558, 543

Bachetti, M., et al. 2014, Nature, 514, 202

Balbus, S. A., & Hawley, J. F. 1991, ApJ, 376, 214

Balbus, S. A., & Hawley, J. F. 1992, ApJ, 400, 610

Barrows, R. S., Mezcua, M., & Comerford, J. M. 2019, ApJ, 882, 181

Begelman, M. C. 1978, MNRAS, 184, 53

Berghea, C. T., Johnson, M. C., Secrest, N. J., Dudik, R. P., Hennessy, G. S., & El-khatib, A. 2020, ApJ, 896, 117

Blaes, O., Krolik, J. H., Hirose, S., & Shabaltas, N. 2011, ApJ, 733, 110

Blandford, R. D., & Znajek, R. L. 1977, MNRAS, 179, 433

Eggum, G. E., Coroniti, F. V., & Katz, J. I. 1988, ApJ, 330, 142

Fujita, M., & Okuda, T. 1998, PASJ, 50, 639

Fukue, J. 2004, PASJ, 56, 569

Fürst, F., et al. 2016, ApJ, 831, L14

Gladstone, J. C., Roberts, T. P., & Done, C. 2009, MNRAS, 397, 1836

González, M., Audit, E., & Huynh, P. 2007, A&A, 464, 429

Gu, W.-M. 2012, ApJ, 753, 118

Hashizume, K., Ohsuga, K., Kawashima, T., & Tanaka, M. 2015, PASJ, 67, 58

Igumenshchev, I. V., & Abramowicz, M. A. 1999, MNRAS, 303, 309

Igumenshchev, I. V., & Abramowicz, M. A. 2000, ApJS, 130, 463

Israel, G. L., et al. 2017, MNRAS, 466, L48

Jiang, Y.-F., Stone, J. M., & Davis, S. W. 2014, ApJ, 796, 106

Jiang, Y.-F., Stone, J. M., & Davis, S. W. 2019, ApJ, 880, 67

Jin, C., Done, C., Ward, M., & Gardner, E. 2017, MNRAS, 471, 706

Kaaret, P., Feng, H., & Roberts, T. P. 2017, ARA&A, 55, 303

Kaaret, P., Ward, M. J., & Zezas, A. 2004, MNRAS, 351, L83

Kato, S., Fukue, J., & Mineshige, S. 2008, Black-Hole Accretion Disks: Towards a New Paradigm (Kyoto: Kyoto University Press)

Katz, J. I. 1977, ApJ, 215, 265

Kawashima, T., Ohsuga, K., Mineshige, S., Heinzeller, D., Takabe, H., & Matsumoto, R. 2009, PASJ, 61, 769

Kawashima, T., Ohsuga, K., Mineshige, S., Yoshida, T., Heinzeller, D., & Matsumoto, R. 2012, ApJ, 752, 18

King, A. R., Davies, M. B., Ward, M. J., Fabbiano, G., & Elvis, M. 2001, ApJ, 552, L109

Kitaki, T., Mineshige, S., Ohsuga, K., & Kawashima, T. 2017, PASJ, 69, 92

Kitaki, T., Mineshige, S., Ohsuga, K., & Kawashima, T. 2018, PASJ, 70, 108

Levermore, C. D., & Pomraning, G. C. 1981, ApJ, 248, 321

McKinney, J. C., Tchekhovskoy, A., Sądowski, A., & Narayan, R. 2014, MNRAS, 441, 3177

Makishima, K., et al. 2000, ApJ, 535, 632

Mihalas, D., & Mihalas, B. W. 1984, Foundations of Radiation Hydrodynamics (Oxford: Oxford University Press)

Miller, J. M., Fabian, A. C., & Miller, M. C. 2004, ApJ, 614, L117

Mineshige, S., Kawaguchi, T., Takeuchi, M., & Hayashida, K. 2000, PASJ, 52, 499

Nakamura, K. E., Kusunose, M., Matsumoto, R., & Kato, S. 1997, PASJ, 49, 503

Narayan, R., Sądowski, A., & Soria, R. 2017, MNRAS, 469, 2997

Narayan, R., & Yi, I. 1994, ApJ, 428, L13

Ogawa, T., Mineshige, S., Kawashima, T., Ohsuga, K., & Hashizume, K. 2017, PASJ, 69, 33

Ohsuga, K., & Mineshige, S. 2007, ApJ, 670, 1283

Ohsuga, K., & Mineshige, S. 2011, ApJ, 736, 2

Ohsuga, K., Mineshige, S., Mori, M., & Kato, Y. 2009, PASJ, 61, L7

Ohsuga, K., Mori, M., Nakamoto, T., & Mineshige, S. 2005, ApJ, 628, 368

Ohsuga, K., & Takahashi, H. R. 2016, ApJ, 818, 162

Paczyński, B., & Wiita, P. J. 1980, A&A, 500, 203

Pakull, M. W., Soria, R., & Motch, C. 2010, Nature, 466, 209

Pietrini, P., & Krolik, J. H. 2000, ApJ, 539, 216

Pinto, C., Middleton, M. J., & Fabian, A. C. 2016, Nature, 533, 64

Press, W. H., Teukolsky, S. A., Vetterling, W. T., & Flannery, B. P. 2007, Numerical Recipes: The Art of Scientific Computing, 3rd ed. (Cambridge: Cambridge University Press)

Rybicki, G. B., & Lightman, A. P. 1986, Radiative Processes in Astrophysics (New York: Wiley)

Sądowski, A., Abramowicz, M., Bursa, M., Kluźniak, W., Lasota, J.-P., & Różańska, A. 2011, A&A, 527, A17

Sądowski, A., & Narayan, R. 2016, MNRAS, 456, 3929

Sądowski, A., Narayan, R., Tchekhovskoy, A., Abarca, D., Zhu, Y., & McKinney, J. C. 2015, MNRAS, 447, 49

Shakura, N. I., & Sunyaev, R. A. 1973, A&A, 24, 337

Shidatsu, M., Ueda, Y., & Fabrika, S. 2017, ApJ, 839, 46

Takahashi, H. R., Mineshige, S., & Ohsuga, K. 2018, ApJ, 853, 45

Takahashi, H. R., Ohsuga, K., Kawashima, T., & Sekiguchi, Y. 2016, ApJ, 826, 23

Turner, N. J., & Stone, J. M. 2001, ApJS, 135, 95

Watarai, K. 2006, ApJ, 648, 523

Watarai, K., Mizuno, T., & Mineshige, S. 2001, ApJ, 549, L77

Yang, X.-H., Yuan, F., Ohsuga, K., & Bu, D.-F. 2014, ApJ, 780, 79